Physica B 598 (2020) 412429

Contents lists available at ScienceDirect

Physica B: Physics of Condensed Matter

journal homepage: http://www.elsevier.com/locate/physb

Role of magnetic anisotropy on the heating mechanism of Co-doped Fe_3O_4 nanoparticles

J. Shebha Anandhi [a], T. Arun [b,c], R. Justin Joseyphus [a,*]

[a] Magnetic Materials Laboratory, Department of Physics, National Institute of Technology, Tiruchirappalli, 620015, India
[b] Advanced Materials Laboratory, Department of Mechanical Engineering, University of Chile, Santiago, 8370456, Chile
[c] Instituto de Investigaciones Científicas y Tecnológicas (IDICTEC), University of ATACAMA, Copiyapo, 1530000, Chile

ARTICLE INFO

Keywords:
Magnetite nanoparticles
Superparamagnetism
Cobalt
Hyperthermia
Magnetic anisotropy
Specific absorption rate

ABSTRACT

The heating characteristics of $Co_xFe_{3-x}O_4$ ($x = 0$, 0.1, and 0.3) nanoparticles of average particle size 10–12 nm were investigated. The electron spin resonance analysis revealed an enhancement in magnetic anisotropy from 16 to 21 kJm^{-3} with low Co doping of $x = 0.1$. Magnetic measurements performed at 15 K showed a coercivity of 290 kAm^{-1} for the $x = 0.1$ composition, that decreased to 37 kAm^{-1} on surface modification. The effective specific absorption rate (ESAR) obtained using infrared thermography demonstrated a decreasing trend from 3.16 to 2.84 nHm^2kg^{-1} due to the increase in magnetic anisotropy associated with Co substitution. An increase in ESAR up to 4.42 nHm^2kg^{-1} was estimated with surface modification of Co-doped Fe_3O_4. The theoretically estimated ESAR considering polydispersity and experimental results presented decreasing behavior with magnetic anisotropy as per the linear response theory.

1. Introduction

Magnetic nanoparticle hyperthermia (MNH) is based on the dissipation of heat when magnetic nanoparticles (MNPs) are exposed to an alternating magnetic field. The heating efficiency of MNPs is evaluated using specific absorption rate (SAR), that are usually undertaken with particle size in the range of 12–14 nm for magnetite (Fe_3O_4) [1–5]. The particle size, being a critical parameter for high heat dissipation, another factor that needs to be optimized for obtaining a better SAR is the magnetic anisotropy constant (K).

$CoFe_2O_4$ having larger K compared to Fe_3O_4 of similar particle size showed reduced SAR [6]. On the other hand, there are also reports that Co substitution in Fe_3O_4 in spite of enhancing the magnetic anisotropy, increases the SAR value [7,8]. The reason for the anomaly in experimental SAR with Co substitution is unclear. It has to be noted that Co-doping enhances the K value due to the spin-orbit coupling induced by the asymmetric distortion of ions [9]. The magnitude of magnetocrystalline anisotropy constant for bulk Fe_3O_4 is 11 kJm^{-3}, whereas it increases with the concentration of Co^{2+} cation, reaches a maximum value with further substitution and then decreases to 200 kJm^{-3} corresponding to $CoFe_2O_4$ [9,10]. Comparison of SAR to evaluate the K dependent heating mechanism requires Co substituted nanoparticles of similar size. Smaller Co^{2+} dopant could substitute Fe^{2+} in the octahedral site enhancing the magnetic anisotropy [9,11] without drastic effects on the particle size and shape. Magnetite is well known for its biocompatibility and is a promising candidate for MNH [2]. Low concentration of Co in Fe_3O_4 is found to tailor the magnetic properties adequately without compromising the cellular biocompatibility. In Co-doped MNPs, cytotoxicity could increase in line with the level of dopant concentration. This drawback could be overcome by coating with suitable surfactants such as chitosan or dextran [6,12].

SAR is influenced by the hysteresis heating that increases with frequency (f) and applied field (H_o), whereas the discomfort factor limits the H_of values to 5×10^9 $Am^{-1}s^{-1}$ [13]. Thus, the effective specific absorption rate (ESAR) is more appropriate for reporting the heating characteristics of MNPs since it considers the inverse dependence on H_o^2f. The importance of evaluating ESAR is seldom brought out, despite the progress in enhancing the SAR. Cobalt ferrite nanoparticles in the size range 7–10 nm showed a wide variation in SAR values from 1.2 to 360 Wg^{-1} [6,14–17]. The difference in the SAR values is attributed to the various applied fields and frequencies in the range of 3–37 kAm^{-1} and 110–700 kHz, respectively. The estimated ESAR of cobalt ferrite from the preceding reports is only in the range of 0.23–1.20 nHm^2kg^{-1}. Even though a higher SAR value of 160 Wg^{-1} has been obtained [15], the

* Corresponding author.
E-mail address: rjustinj@nitt.edu (R.J. Joseyphus).

https://doi.org/10.1016/j.physb.2020.412429
Received 3 June 2020; Received in revised form 23 July 2020; Accepted 1 August 2020
Available online 10 August 2020

computed ESAR of 0.23 nHm^2kg^{-1} is the lowest due to the large applied field of 37 kAm^{-1}.

Co substituted Fe_3O_4 ($0.5 \leq x \leq 1$) of average size 16–20 nm exhibited SAR of 316–420 Wg^{-1} and the calculated ESAR is less than 1.5 nHm^2kg^{-1} [18,19]. Verde et al. [20] reported reduced SAR with enhanced K (26–42 kJm^{-3}) that resulted in an ESAR of 0.01 nHm^2kg^{-1} for $0.7 \leq x \leq 1$. Conversely, studies by Fantechi et al. [7] showed an increase in SAR with Co-doping up to $x = 0.6$, whereas the ESAR is only 0.25 nHm^2kg^{-1}. An increase in K from 15 to 570 kJm^{-3} was observed, which was correlated to the enhancement in SAR due to Co-doping. Similar SAR behavior was obtained with higher K values (80 kJm^{-3} to 17×10^5 Jm^{-3}) in the Co-doped samples, as reported by Mohapatra et al. [8]. The SAR values reported in the literature show an increasing trend with K in Co-based nanoparticles in contrast to the linear response theory (LRT) [7,8,21]. Moreover, it was shown that ESAR increased to 2.37–3.32 nHm^2kg^{-1} (K = 15–17 kJm^{-3}) with Mn-doping in Fe_3O_4 at lower concentrations [22]. Although substantial variation in K was not achieved with Mn-doping, the low concentration of Co in Fe_3O_4, especially $x \leq 0.3$, is expected to show significant variation in K and hence in the heating characteristics.

Apart from the physical properties that influence the heating characteristics, the choice of the thermal probe is also important in experimental MNH. Infrared thermography (IRT) is a non-invasive technique used to obtain SAR values from a broad sample area with considerable sensitivity, avoiding multiple thermal probes for real-time monitoring [23–25]. Indeed, the interference of radiative heating from the coil could be easily comprehended using IRT, unlike contact methods. The heating efficiency determined using IRT and the ESAR has advantages over contact methods and SAR, respectively, for practical applications. This study aims to understand the magnetic anisotropy dependent ac magnetic heating mechanism with low Co-doping in Fe_3O_4 using IRT. The effect of K and the particle size distribution on ESAR has been estimated theoretically and compared with the experimental results.

2. Materials and methods

2.1. Synthesis

$Co_xFe_{3-x}O_4$ (x = 0, 0.1, and 0.3) nanoparticles were synthesized using the conventional co-precipitation method with cobalt (II) chloride, iron (II) chloride tetrahydrate, anhydrous ferric chloride, and sodium hydroxide. The magnetite sample used for comparison is similar to our previous reports [22,23]. The reactants dissolved in deionized water with appropriate molar ratios (total of 1.1 M) were heated to 353 K under magnetic stirring and the temperature was maintained for an hour. The precipitated nanoparticles were magnetically separated and are labelled as Co0, Co1, and Co3, referring to Fe_3O_4, $Co_{0.1}Fe_{2.9}O_4$, and $Co_{0.3}Fe_{2.7}O_4$, respectively.

Surface modification of the $Co_{0.1}Fe_{2.9}O_4$ nanoparticles was implemented *ex-situ* using dextran (MW 10 kDa). The dextran modified samples were sonicated for different durations before drying in an air oven at 353 K. The surface-modified $Co_{0.1}Fe_{2.9}O_4$ samples are labelled based on the sonication time of 10 min and 2 h as D-Co1 and D2-Co1, respectively.

2.2. Characterization

The X-ray diffraction (XRD) patterns were obtained using a Rigaku Ultima III X-ray diffractometer with Cu-Kα. Transmission electron microscopy (TEM) was performed with FEI make, Tecnai F20 - 200 kV TEM. The cobalt content in the doped sample was affirmed using inductively coupled plasma – atomic emission spectroscopy (ICP-AES) model ARCOS, simultaneous ICP spectrometer. The Co content obtained from ICP-AES analysis is in close agreement with the initial concentration. The magnetic anisotropy was estimated from an electron spin resonance (ESR) spectrometer (JEOL, model JES FA200) in the X band frequency range at room temperature (RT). The RT and low-temperature magnetic measurements were undertaken using Lakeshore model 7404 vibrating sample magnetometer (VSM). Temperature-dependent weight loss curves were obtained from the thermogravimetric analysis (TGA) measured using EXSTAR 6200 TG/DTA. The Curie temperatures were estimated from the thermomagnetic analysis (TMA) by applying an external magnetic field.

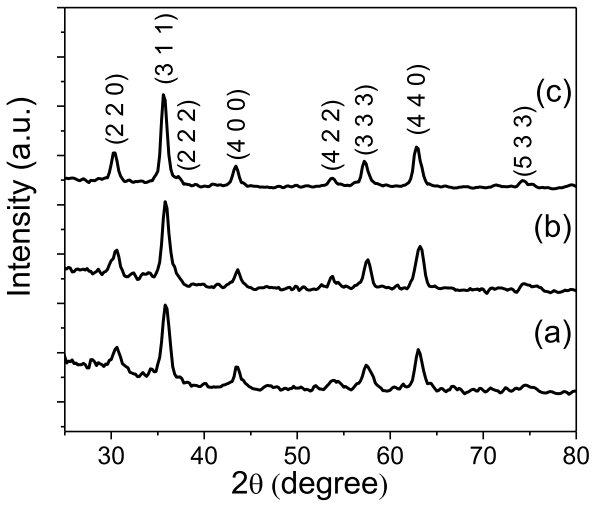

Fig. 1. XRD patterns of (a) Co0, (b) Co1, and (c) Co3.

The heating studies were performed using a radiofrequency (rf) generator with a magnetic field strength of 4 kAm^{-1} and a frequency of 500 kHz. The thermal images were captured using a thermographic camera (Thermo Shot F 30), having a resolution of 0.1 K in the long-wave infrared region. The ESAR evaluation of the samples and the experimental steps were undertaken similar to our previous report using IRT [23]. In a typical experimental procedure, 40 mg of nanoparticles were dispersed in 1 ml deionized water. The sample holder has a diameter of 2 cm, corresponding to a sample area density of 3.3 kgm^{-2}. The rf generator comprised a two-turn water-cooled coil with a diameter of 5.2 cm and the sample holder was placed at the coil center. The calibration of the thermography camera was undertaken as per standard procedure and the average temperature was compared with conventional probes. The thermography patterns were recorded for a time period of 180 s.

3. Results and discussion

Fig. 1 shows the XRD patterns of (a) Co0, (b) Co1, and (c) Co3. The (hkl) values of the samples are in agreement with the JCPDS data (file no. 821533) corresponding to Fe_3O_4 with fcc (face-centered cubic) structure. The average grain sizes are 10(1), 11(1), and 12(1) nm for Co0, Co1, and Co3, respectively. It is evident that Fe_3O_4 and Co-doped Fe_3O_4 samples are devoid of impurities and possess closer average grain sizes. The lattice parameters for Co0, Co1, and Co3 are found to be 8.334(5), 8.319(5), and 8.337(5) Å, respectively. The lattice parameter for Co0 is in concurrence with the value of 8.33 Å obtained by Pati et al. [26] for their magnetite sample prepared using the co-precipitation method. The slight decrease in the lattice parameter of Co1 may be due to the smaller ionic radius of Co^{2+} (0.74 Å) that substitutes in the Fe^{2+} (0.77 Å) lattice sites [27]. The results are in agreement with the report by Fantechi et al. [7], where a reduction in lattice parameter was observed up to 7% Co substitution and increased thereafter. It is to be noted here that the lattice parameter may vary based on the synthesis conditions that result in surface distortion and changes in cation distribution. Yang et al. [28] suggested a decrease in the lattice parameter by 0.2 Å per vacancy. The other factors reported to affect the lattice parameter are surface oxidation, lattice strain due to the large surface to

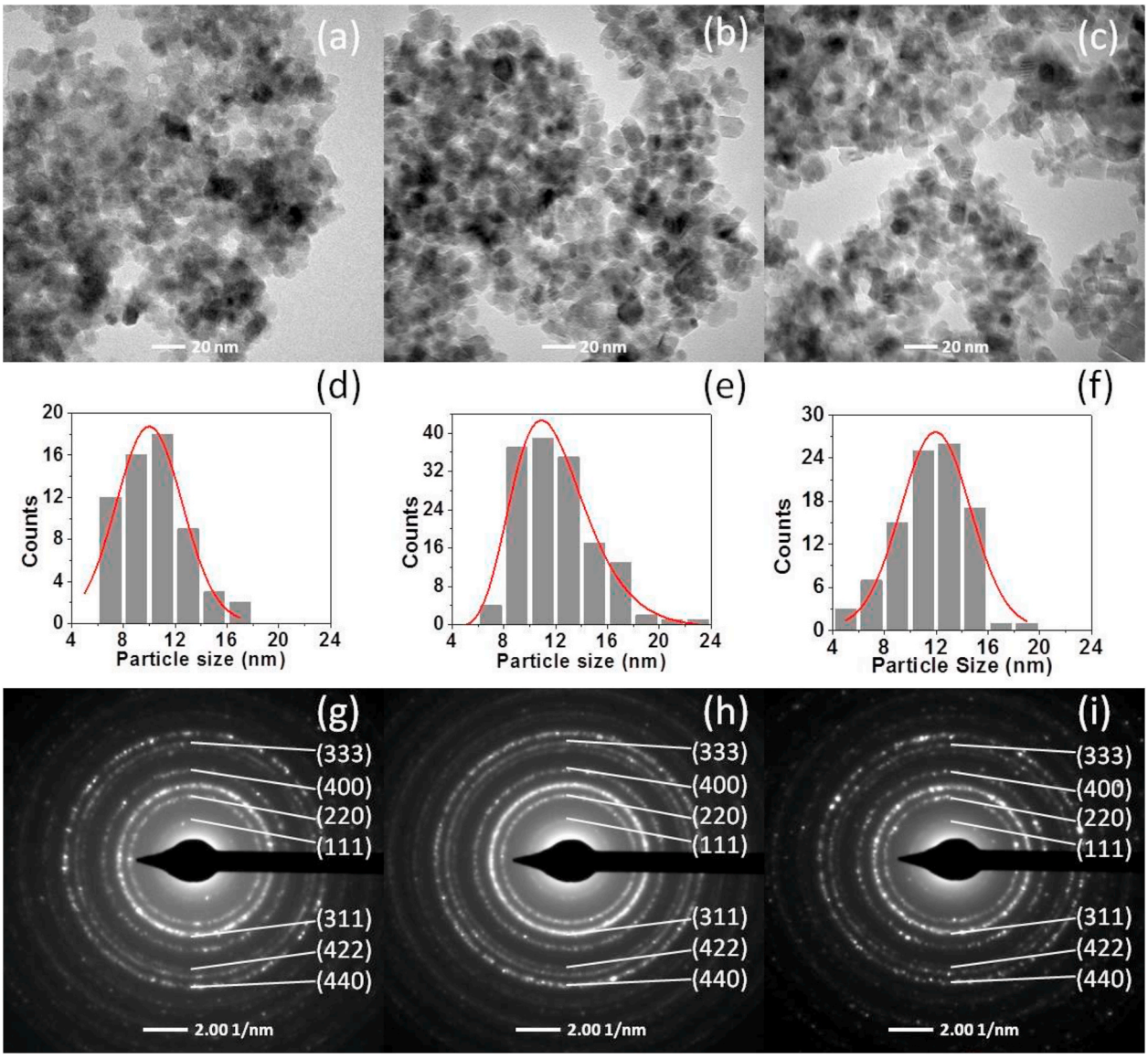

Fig. 2. TEM images of (a) Co0, (b) Co1, and (c) Co3 with their particle size distribution histograms (middle row) and SAED patterns (bottom row).

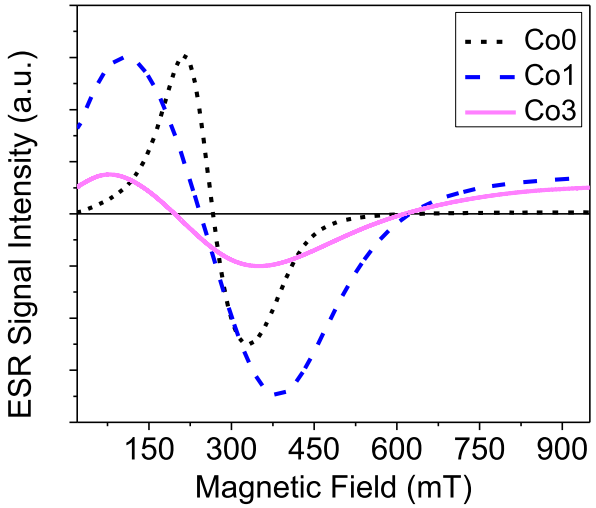

Fig. 3. ESR spectra corresponding to Co0, Co1, and Co3.

volume ratio and cation distribution [11,29,30].

Fig. 2 shows the TEM images of (a) Co0, (b) Co1, and (c) Co3 with their corresponding particle size distributions (middle row) and SAED patterns (bottom row). The TEM images show particles in the size range of 4–24 nm for Co0, Co1, and Co3, where the average particle sizes are in the closer range of 10–12 nm. The SAED patterns show lattice planes corresponding to the fcc structure of Fe_3O_4. The lattice parameters obtained from SAED for Co0, Co1, and Co3 are 8.333(5), 8.317(5), and 8.336(5) Å, respectively. The lattice parameters are in close agreement with the results obtained from XRD.

The magnetic anisotropy constant can be obtained from ESR in which the magnetic materials respond to the microwave excitations in applied fields [31,32]. Fig. 3 shows the ESR spectra of Co0, Co1, and Co3 at room temperature. The spectrum for Co0 is sharp and symmetrical, while a tenuous broadening is witnessed in Co1. Co3 displays a substantial broadening, where the augmentation in broadening with Co substitution arises due to the enhanced ferromagnetic interactions between adjacent spins induced by the high magnetic anisotropy of Co [33–35]. The magnetic anisotropy constant was calculated from $H_A = \frac{2K}{M_s}$, where H_A is the anisotropy field obtained from the angular resonant frequency, $\omega_o = \gamma_e H_A$ with the gyromagnetic ratio, $\gamma_e = 2.002 \times 10^5$

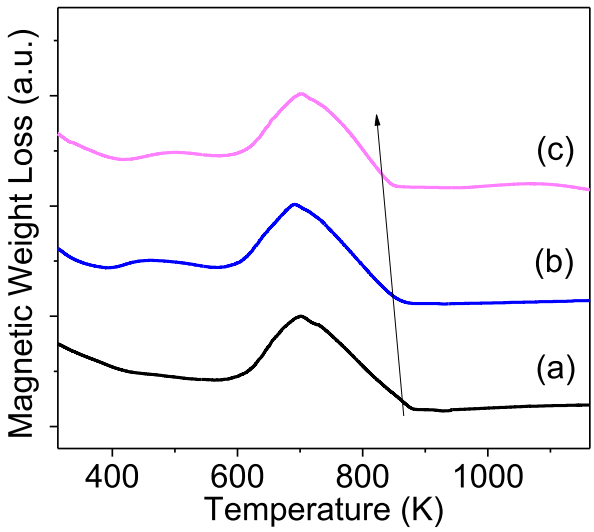

Fig. 4. Temperature-dependent magnetic weight loss curves of (a) Co0, (b) Co1, and (c) Co3.

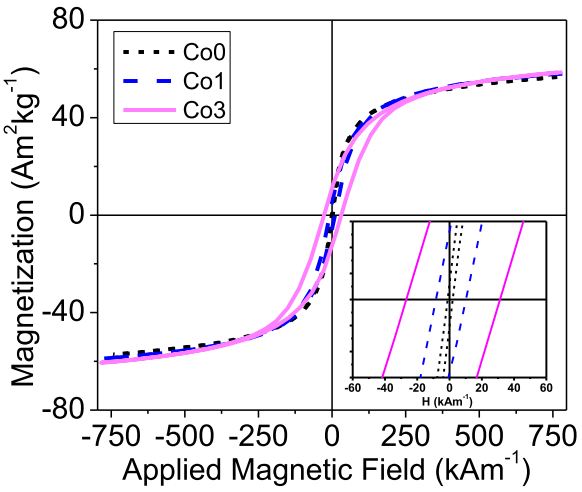

Fig. 5. Room temperature hysteresis loops of Co0, Co1, and Co3. Inset shows the magnified low field region of the hysteresis loops.

mA^{-1}s^{-1} and K is the effective magnetic anisotropy [36,37].

The K value obtained in our study is 16 kJm^{-3} for Co0, which is close to 15 kJm^{-3} estimated by Fantechi et al. [7] in the size range of 8–9 nm prepared by thermal decomposition method. Owing to the presence of surface anisotropy in the MNPs, the obtained K values are usually higher than the bulk values [38,39]. The K values for Co1 and Co3 are 21 and 31 kJm^{-3}, respectively, which arise from the intrinsic contribution of Co-doping. Although our attempt with a higher concentration ($x = 0.5$) enhanced the K to 25 kJm^{-3}, it was lower than $x = 0.3$ due to negligible surface anisotropy, as the average particle size was much larger about 40 nm resembling asymmetric flakes. Few of the reports in Co-based nanoparticles are not comparable since the estimated K is as high as 17×10^5 Jm^{-3}, which probably could be an outcome of variant synthesis conditions, composition, and particle size [8,40]. The K values of 26–42 kJm^{-3} reported for $Co_xFe_{3-x}O_4$ (x = 0.7 to 1) synthesized using the co-precipitation method with particle sizes between 13 and 14 nm [20] are reasonably closer to our values. The K value is influenced by the occupancy of Co^{2+} in either octahedral (B) or tetrahedral site (A) that undergoes asymmetric distortion and changes in the spin-orbit energy [9,41,42]. The K value also plays an important role in determining the critical superparamagnetic size.

The critical superparamagnetic volume of MNPs can be evaluated using the expression

$$V = \frac{25 k_B T_B}{K} \quad (1)$$

where k_B is the Boltzmann constant and T_B is the blocking temperature [10]. Using Eq. (1) with the K values obtained from ESR, the calculated T_B values are 50, 110, and 160 K for Co0, Co1, and Co3, respectively. With Co-doping, the T_B value usually increases, as reported by Fantechi et al. [7] and Mohapatra et al. [8]. The T_B values suggest that all the samples are superparamagnetic at 300 K, a condition required for heat generation as per the linear response theory [21]. The critical superparamagnetic size (D_{spm}) was also computed employing Eq. (1) with T_B as 300 K. The D_{spm} for Co0, Co1, and Co3 are 23, 21, and 18 nm, respectively. It is apparent that all the samples are superparamagnetic at room temperature, with average particle sizes well below the critical D_{spm}.

Fig. 4 shows the temperature-dependent magnetic weight loss curves of (a) Co0, (b) Co1, and (c) Co3. The magnetic weight loss corresponds to the weight loss encountered by a magnetic sample under the influence of an applied magnetic field in a TGA. All samples show a considerable weight gain, known as the Hopkinson peak [43,44] followed by weight loss corresponding to the Curie temperature (T_c) of the samples. The T_c is found to decrease with Co-doping exhibiting 863, 857, and 849 K, corresponding to Co0, Co1, and Co3, respectively. While the T_c of Co0 is close to the bulk Fe_3O_4 value of 858 K, the values of Co-doped Fe_3O_4 samples decrease towards the bulk $CoFe_2O_4$ value of 793 K [10]. Substituting a smaller concentration of Co corresponding to $x = 0.03$ in Fe_3O_4 decreases the T_c by 10 K [45]. Nevertheless, T_c was found to decrease noticeably with Co-doping, as seen in our study, that may be correlated to the reduction in the intersublattice exchange coupling between A and B sublattices.

The hysteresis curves of Co0, Co1, and Co3 were investigated at 300 K (Fig. 5) with a maximum field of 800 kAm^{-1}. The magnified region of room temperature coercivity for all the samples is shown as an inset in Fig. 5. The saturation magnetization (M_s) values of all samples are nearly 58(2) Am^{2}kg^{-1}. The observed M_s is lower than the bulk value of 92 Am^{2}kg^{-1} due to the surface spin effects attributing to the smaller particle size [10,46]. The hysteresis exhibited by Co0 is characteristic of superparamagnetic nanoparticles with a low coercivity (H_c) of 1 kAm^{-1} consistent with the lowest K. The H_c values increase for Co1 and Co3 to 8 and 27 kAm^{-1}, respectively. Though Co1 and Co3 show comparatively larger coercivity, the T_B values estimated from ESR show that they are superparamagnetic in nature. Since a distribution in sizes is witnessed in all samples, the particles beyond the critical superparamagnetic regime could have contributed to the augmentation of magnetic anisotropy that resulted in enhanced coercivity in Co-doped Fe_3O_4. The coercivity reported for $x = 0.2$ was 9 kAm^{-1}, which enhanced with Co-doping and reached a maximum of 24 kAm^{-1} for $x = 1$ [47]. For x between 0.1 and 0.4, M_s and H_c values were reported as 74–78 Am^{2}kg^{-1} and 28-47 kAm^{-1}, respectively [27]. The Co-doped Fe_3O_4 ($0.7 \leq x \leq 1$) in the size range of 13–14 nm showed an increase in H_c from 21 to 44 kAm^{-1} compared to the undoped sample of similar size [20]. These studies point to the enhancement in coercivity with Co-doping, as observed in our measurements.

Though Co1 and Co3 possess the same average particle size of 12 nm, Co1 presents lower coercivity, and K when compared with Co3. Since low dopant concentration is preferred from the biocompatibility aspect, Co1 is suitable for surface modification. However, surface modification would influence the dipolar interactions [23]. Hence, to examine the effect of dipolar interactions, Co1 was *ex-situ* surface modified using dextran and the influence of interaction was studied with different sonication times. Larger sonication duration would induce much better particle separation and dispersion as in D2-Co1.

The TGA curves of Co1, D-Co1, D2-Co1, and pure dextran are shown in Fig. 6. In the case of pure dextran, the decomposition primarily takes

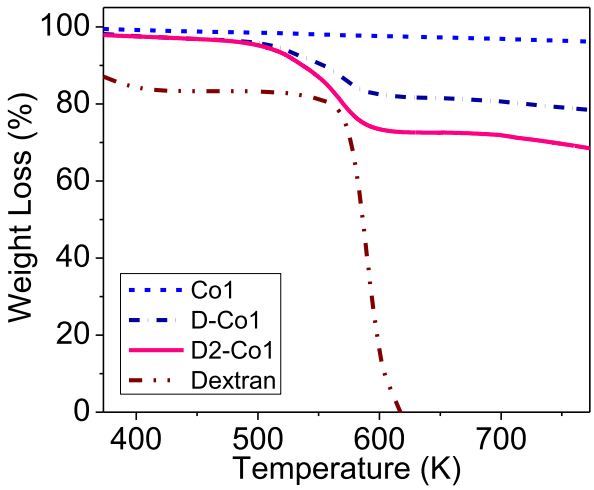

Fig. 6. TGA curves of Co1, D-Co1, D2-Co1, and pure dextran.

place in the range 533–593 K. The weight losses for D-Co1 and D2-Co1 witnessed in the same range are 10% and 20%, respectively, whereas, for the uncoated Co1, the curve is almost flat with no sign of physical or chemical change. Therefore the presence of dextran in the *ex-situ* coated samples (D-Co1 and D2-Co1) is confirmed from the TGA curves.

The investigation of hysteresis curves of D-Co1 and D2-Co1 at 300 K (Fig. 7(a)) and those of Co0, Co1, D-Co1, and D2-Co1 at 15 K (Fig. 7(b)) were carried out with a maximum field of 800 kAm^{-1}. The magnified region of RT coercivity for D-Co1 and D2-Co1 is shown as an inset in Fig. 7(a). The M_s for D-Co1 and D2-Co1 at 300 K are 53(2) and 46(2) Am^2kg^{-1}, respectively. The M_s values are lower than the unmodified samples due to the presence of non-magnetic dextran.

At 300 K, the H_c of D-Co1 and D2-Co1 are 4 and 0.8 kAm^{-1}, respectively. The decrease in H_c with the sonication time and with dextran suggests that the particles are well separated where interparticle interactions are reduced [48,49]. From Fig. 7(b), the irreversible behavior below the blocking temperature is evident at 15 K, which explains the increase in H_c value of 27 kAm^{-1} for Co0. Though the hysteresis curves of Co0 and Co1 at RT (Fig. 5) look similar, at low-temperature, the H_c adopts a sharp increase (Fig. 7(b)) with a small amount of Co-doping. A comparatively higher H_c of 290 kAm^{-1} at 15 K was obtained for Co1 due to the drastic increase in the low-temperature magnetocrystalline anisotropy. Since particles are aggregated in the absence of dextran, the larger anisotropy energy (KV) results in the enhancement of coercivity [50].

The H_c for D-Co1 and D2-Co1 at 15 K are 246 and 37 kAm^{-1}, respectively. D2-Co1 at 15 K (Fig. 7(b)) exhibits a constricted hysteresis loop near zero applied fields. The dipolar interactions play an increasingly important role in explaining the shape of hysteresis [51]. The reason for this behavior is explained by Lee et al. [52], as observed for $L1_0$ FePt coated with SiO_2. The abrupt relaxation of magnetic moments arises when the applied field is reversed in D2-Co1, unlike Co1 and D-Co1. This kind of abrupt relaxation can be ascribed to the distribution in size or composition of the sample, which is generally found in samples with a combination of soft and hard magnetic phases.

The MNPs with random orientations rotate in the applied field direction, which explains the gradual rise in magnetization in higher field regions. On the other hand, the moments relax to their easy axes as the field is reduced to zero. Furthermore, coercivity is related to surface modification as the dextran layers weaken the magnetic dipolar coupling between the MNPs and lead to increased interparticle separation [53,54]. Fig. 8 illustrates the dipolar interactions between (a) unmodified and (b) surface modified MNPs in an applied magnetic field. The interparticle distance (d) affects the magnetic response such that with an increase in interparticle separation, the dipolar interaction is diminished [51]. In the absence of the applied field, uncoated MNPs tend to agglomerate due to the dipolar coupling between the particles. At very low temperatures, the presence of the field makes the strongly

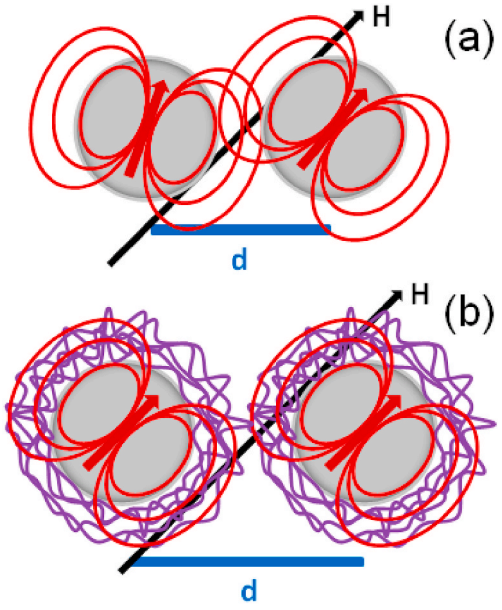

Fig. 8. Dipolar interactions between (a) unmodified and (b) surface modified MNPs in an applied magnetic field.

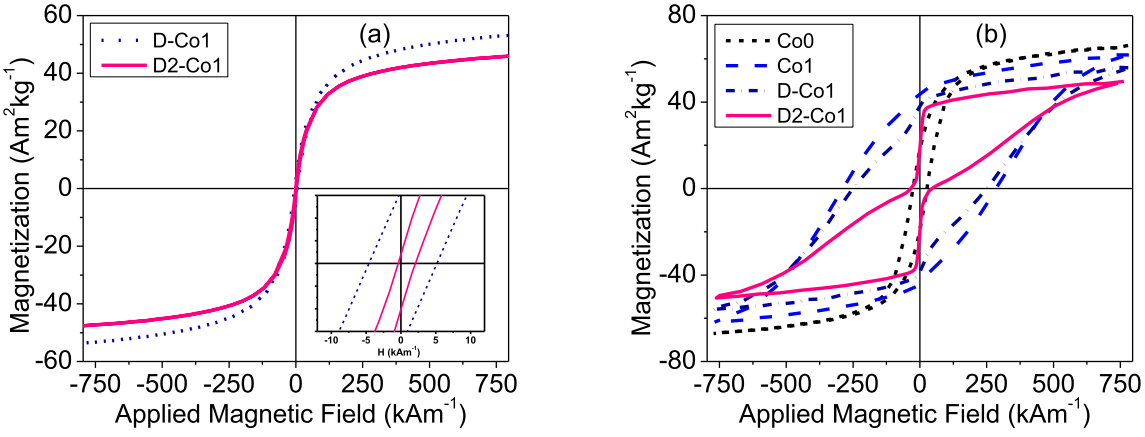

Fig. 7. Hysteresis loops of Co1 and the surface-modified samples at (a) 300 K and at (b) 15 K along with Co0.

dipolar system more stable by enhancing the H_c, as observed by Blanco-Andujar et al. [55], which is also witnessed in Co1 at 15 K.

With surface modification, the dipolar coupling between the particles is forbidden that ensued in lessening the effects of dipolar interaction, allowing the MNPs to rotate freely in the direction of the applied field, thereby resulting in constricted hysteresis for D2-Co1 (Fig. 7(b)). This effect, to an extent, is observed in D-Co1, which explains the slight constriction close to the zero-field regions. This probably could be due to the short sonication time where the agglomerated particles got trapped within the dextran threads rather than individual particles during *ex-situ* surface modification. Though dextran offers a slight constriction, the dipolar coupling of the agglomerated particles gives rise to large coercivity. It is to be noted here that the particles are superparamagnetic at room temperature, and therefore, the low-temperature magnetic properties shall give further information about the particles.

The ratio between remanence (M_r) and M_s is given as the squareness ratio, $R = (M_r/M_s)$. At 15 K, R for Co0 is 0.2, which is less than the theoretical value of 0.5 estimated by the Stoner-Wohlfarth model [10]. Theoretical simulations by Kechrakos and Trohidou [51], have suggested that R decreases drastically below 0.5 when the anisotropy energy decreases. Since the Co0 sample has lower anisotropy energy than Co1, the R value is reduced to 0.2. R for Co1 and D-Co1 is 0.7, which is the characteristic of an assembly of MNPs coupled to each other by dipole-dipole interactions [56]. On the other hand, for D2-Co1, the R value is 0.4, which indicates the reduction in the dipolar interaction with prolonged sonication that separates the particles.

Although the MNPs which meet the requirement for tumor ablation is established considerably, the heating mechanism of the MNPs suitable for MNH is being pursued rigorously [4,7,8,21,23,57–63]. The total power dissipation in a magnetic material can arise due to various losses such as hysteresis, eddy current, and anomalous losses. For hyperthermia applications, single-domain MNPs are only preferred, and eddy current losses are negligible in these particles [5,64]. Carrey et al. [21] reported that while evaluating the power dissipation factor, the separation between hysteresis loss and Néel-Brown relaxation loss should not be undertaken. The hysteresis losses in single-domain MNPs can be accounted for by applying the LRT for superparamagnetic nanoparticles and Stoner-Wohlfarth model (SWM) for the ferromagnetic nanoparticles. It is to be accentuated that the superparamagnetic particles have to be in the optimum size as per the Rosensweig model for maximum power dissipation [5].

The power dissipation of MNPs due to the Néel-Brown relaxation mechanism in an alternating magnetic field is expressed as

$$P_{NB} = \pi\mu_o\chi_o H_o^2 f \frac{(2\pi f\tau)}{1+(2\pi f\tau)^2} \tag{2}$$

where μ_o, χ_o, H_o, f, and τ are the permeability of free space, susceptibility, applied field strength, frequency, and effective relaxation time, respectively.

The Néel (τ_N) and Brownian (τ_B) relaxation times are given by the following equations,

$$\tau_N = \frac{\sqrt{\pi}}{2}\tau_o\frac{\exp(\sigma)}{\sqrt{\sigma}} \tag{3}$$

$$\sigma = \frac{KV_M}{k_B T} \tag{4}$$

$$\tau_B = \frac{3\eta V_H}{k_B T} \tag{5}$$

where τ_o is the relaxation time constant, V_M is the magnetic particle volume, T is the temperature, η is the viscosity of the medium, and V_H is the hydrodynamic volume of MNP [5].

The specific absorption rate, also known as the specific loss power (SLP) of the MNPs represented in Wg^{-1} is not suitable for comparison since the dependence on the frequency and the square of the applied field is not taken into consideration. This drawback can be overcome by evaluating the ESAR or intrinsic loss power (ILP) expressed in $Wg^{-1}Oe^{-2}Hz^{-1}$ or nHm^2kg^{-1} [23,55,65–68]. The difference could be understood from the fact that although SAR of Co ferrite reported is 145 Wg^{-1}, the ESAR is only 0.34 nHm^2kg^{-1} [17]. The computed ESAR is low due to the large applied field and frequency of 25 kAm^{-1} and 700 kHz, respectively. On the other hand, when f and H_o are intermediate at about 260 kHz and 13 kAm^{-1}, respectively, the SAR values tend to be in the range of 80–140 Wg^{-1} while the ESAR values are 1.92–3.26 nHm^2kg^{-1} [69].

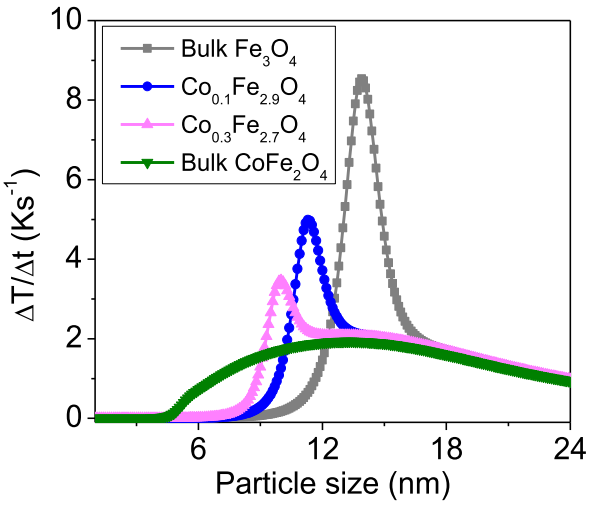

Fig. 9. Theoretical heating rate as a function of particle size of Fe_3O_4, $Co_{0.1}Fe_{2.9}O_4$, $Co_{0.3}Fe_{2.7}O_4$, and $CoFe_2O_4$.

The ESAR values could be obtained using Eq. (6) as

$$\text{ESAR} = \frac{\Sigma_i c_i m_i}{m_{MNP}}\frac{\Delta T}{\Delta t}\frac{1}{H_o^2 f} \tag{6}$$

where c is the specific heat capacity taken as 670 and 4186 $Jkg^{-1}K^{-1}$ for $c_{Fe_3O_4}$ and c_{H_2O}, respectively, m is the mass of each component, m_{MNP} is the mass of the magnetic nanoparticles, and $\Delta T/\Delta t$ is the initial slope of the time-dependent heating profile. The small amount of doping with Co does not alter the specific heat capacity substantially and hence c for Co1 and Co3 is also taken as 670 $Jkg^{-1}K^{-1}$. The product of the applied field and frequency, $H_0 f$ is 2×10^9 $Am^{-1}s^{-1}$, and it falls within the allowed limit of electromagnetic radiation for biomedical applications.

Fig. 9 shows the comparative theoretical heating rates of Fe_3O_4, $Co_{0.1}Fe_{2.9}O_4$, $Co_{0.3}Fe_{2.7}O_4$, and $CoFe_2O_4$ with the applied field and frequency of 4 kAm^{-1} and 500 kHz, respectively. The K values of $Co_{0.1}Fe_{2.9}O_4$ and $Co_{0.3}Fe_{2.7}O_4$ obtained from the ESR studies were used in the calculation, while bulk values are considered for the others. The major difference between the heating curves arises due to the magnetic anisotropy constant. It is apparent that the heating rate decreases with an increase in K when the MNPs comply with the LRT. In addition, the optimum radius suitable for high power dissipation shifts towards smaller sizes with an increase in K. This could be observed from Fig. 9, where the optimum sizes for maximum heating rate are found to be 14, 11, and 10 nm for Fe_3O_4, $Co_{0.1}Fe_{2.9}O_4$, and $Co_{0.3}Fe_{2.7}O_4$, respectively. It is to be noted here that the intensity of the heating rate decreases with K, whereas the fraction of particles generating heat from the distribution in size increases.

Fig. 10 (left) shows the experimental thermal patterns of (a) Co0, (b) Co1, (c) Co3, and (d) D2-Co1 at $t = 0$ s (left panel) and (e) to (h) at $t =$ 180 s (right panel). The rf induced heating of the samples could be seen from the central high-temperature region at $t = 180$ s where the samples are located. The heating from the coil did not interfere with the heat

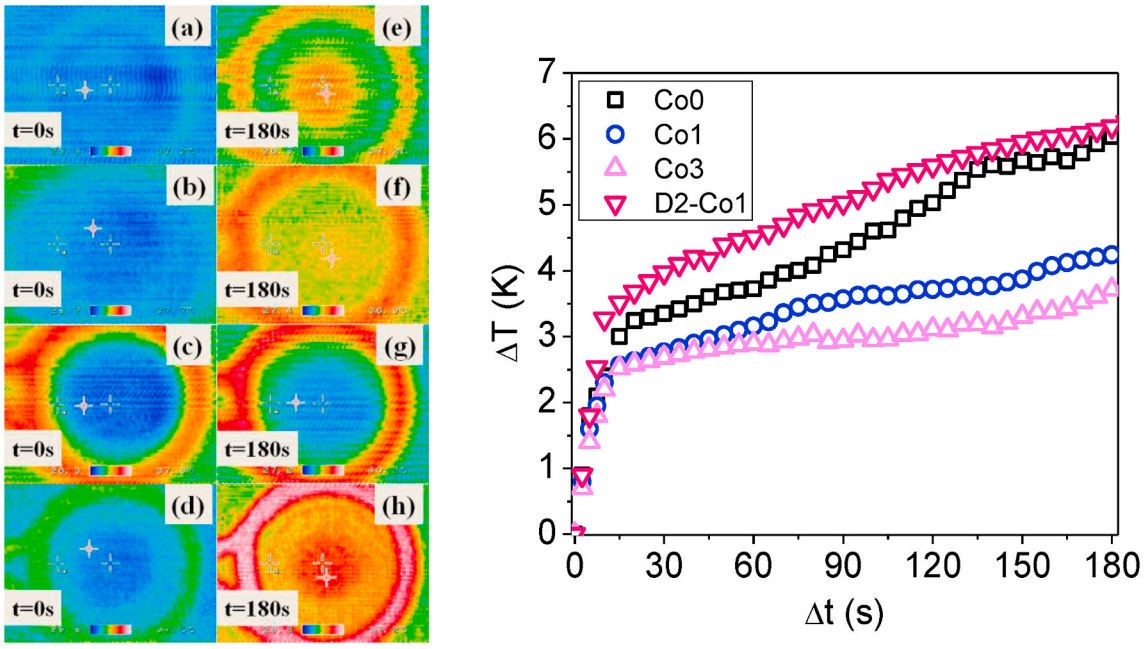

Fig. 10. Thermograms of (a) Co0, (b) Co1, (c) Co3, and (d) D2-Co1 at $t = 0$ s and the respective samples (e) to (h) at $t = 180$ s (left). Time-dependent heating characteristics of Co0, Co1, Co3, and D2-Co1 (right).

generated by the samples, as depicted in Fig. 10 (left). Co0 and D2-Co1 presented significant heating, as shown in the thermograms, whereas Co3 exhibited the least heating. The decrease in heating with Co-doping can be witnessed from the thermal image of Co3 (Fig. 10(g)). Also, the enhancement in heating with surface functionalization (D2-Co1) can be distinctly observed.

The convection losses can give rise to inhomogeneity in the experimental determination of initial heating rates. Studies by Rodrigues et al. [25] have shown an agreement between thermography and the fiber optic measurements within a 5% error, where the discrepancy was related to the skin emissivity angle of dependence in the experimental setup. Lahiri et al. [70] explicitly studied the difference between the fiber optic temperature sensor and IRT and showed that the SAR obtained using the latter was higher owing to the convection losses. They had also shown that the error was reduced to less than 5% when the convection loss correction was applied to the IRT based results. The proximity of initial heating rates employing fiber optic thermometer and IRT was reported by Lahiri et al. [24], where the dissimilarity commenced after a specific time interval. The above reports show that the measurement protocol, including the emplacement of the IR camera, also plays a crucial role in subduing the errors due to convection losses that must be scrupulously enforced while evaluating the heating characteristics. The convection correction was applied to the samples and the error calculated for Co0, Co1, and Co3 are 3, 2, and 2%, respectively, which are within the 5% limit obtained by Lahiri et al. [70].

Another essential aspect that has to be noted is the uncertainty that may arise during the ac field-induced non-adiabatic heating. Understanding the thermodynamic uncertainties like peripheral heating, delayed heating, and spatial variation of temperature profile within the sample is essential for acquiring reliable and reproducible SAR. It was observed by Lahiri et al. [71] that when the coil temperature was low, inhomogeneity in the temperature of the medium also reduced. From the comparison of data obtained from fiber optic sensor and IRT, delay in heating was prominent in the measurements employing the former and uncertainty of nearly 1% may arise from the spatial variations. All these parameters are to be prudently weighed while probing the hyperthermia efficiency utilizing IRT.

The heating characteristics of Co0, Co1, Co3, and D2-Co1 for a time period of 180 s plotted from the thermograms are shown in Fig. 10 (right). D2-Co1 showed the highest heating, while Co3 showed the lowest among the samples under study. The heating rate of the unmodified samples was found to decrease with Co-doping. The SAR and corresponding ESAR of Co0 are 25 Wg^{-1} and 3.16 nHm^2kg^{-1}, respectively. The ESAR of Co0 is consistent with the values reported in the literature for Fe_3O_4 nanoparticles synthesized via co-precipitation route [4,72], whereas it is only 0.33 nHm^2kg^{-1} for the sample of similar size (11 nm) synthesized through thermal decomposition method. The higher SAR of 132 Wg^{-1} [8] is a result of a very high H_o of 39 kAm^{-1}, which when normalized, resulted in a poor ESAR (0.33 nHm^2kg^{-1}). The SAR for Co1 and Co3 are 24 and 23 Wg^{-1}, respectively. The ESAR for Co1 is 3.00 nHm^2kg^{-1}, which is higher than 0.49 nHm^2kg^{-1} (SAR = 200 Wg^{-1}, $H_o = 39$ kAm^{-1}, $f = 265$ kHz) reported for the sample of similar size synthesized via thermal decomposition [8]. The Co0, Co1, and Co3 exhibited ESAR of 3.16, 3.00, and 2.84 nHm^2kg^{-1}, respectively, showing a decreasing trend with Co substitution as per LRT. The LRT is valid for the particles in the superparamagnetic regime if $\xi < 1$, where $\xi = \frac{\mu_o M_s V_M H_o}{k_B T}$ is a dimensionless parameter [21,22]. All the samples in this study have ξ between 0.4 and 0.6. For $\xi > 1$, LRT is no longer applicable, and the SWM is only pertinent for the MNPs in the ferromagnetic regime.

The ESAR for D-Co1 and D2-Co1 are estimated to be 3.63 and 4.42 nHm^2kg^{-1}, respectively. D2-Co1 showed better heating due to the larger interparticle separation that reduces the dipolar interaction affecting the Néel relaxation time [73–77]. In a previous report, 11 nm dextran modified Fe_3O_4 nanoparticles exhibited an ESAR of 5.68 nHm^2kg^{-1} [23], whereas surface-modified 7 nm cobalt ferrite showed 2.90–3.22 nHm^2kg^{-1} [78]. The reduction in ESAR with Co-doping is also apparent in the surface-functionalized superparamagnetic nanoparticles that adhere to LRT. In the presence of dipolar interaction, the mean-field model [79] suggests the modification of the anisotropy energy barrier which is given as

$$\sigma_{eff} = \sigma + \gamma\sigma^2 \tag{7}$$

where σ_{eff} replaces σ in Eq. (4) and

$$\gamma = \frac{9N}{100}\left(\frac{\mu_o\mu^2}{4\pi K V_M}\right)^2\left(\frac{1}{d^6}\right) \tag{8}$$

Here, N is the total number of particles in the system, μ is the

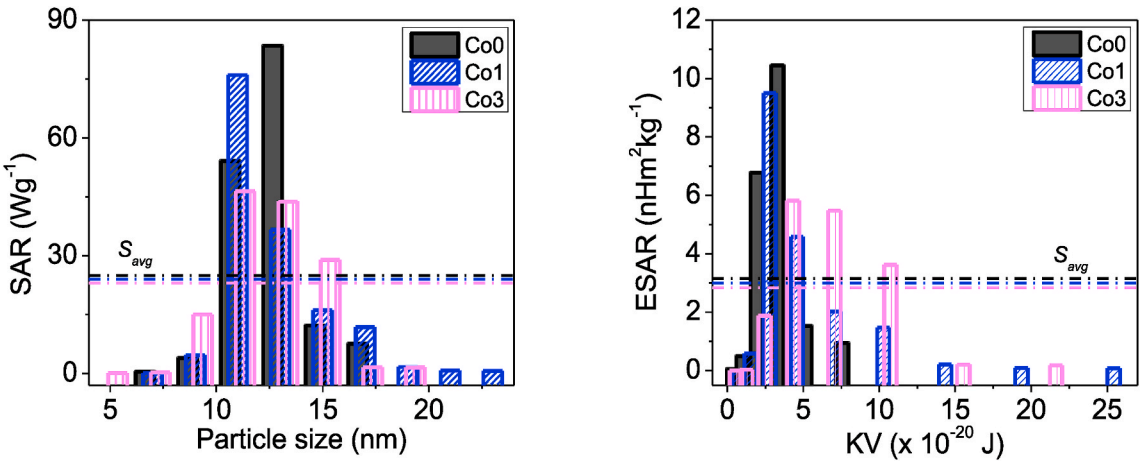

Fig. 11. Theoretical estimation of (a) SAR vs. particle size and (b) ESAR vs. anisotropy energy for polydispersed Co0, Co1, and Co3.

magnetic moment, and d is the interparticle distance, as illustrated in Fig. 8. Thus, the dipolar interaction term, which is highly dependent on the interparticle distance, in turn, will affect the Néel relaxation time given in Eq. (3).

As polydispersity is always present during the synthesis of MNPs, it has a deciding role to play in the heating characteristics besides optimum size and suitable anisotropy. Hence, theoretical simulations of the samples under study were executed for the particle size distributions obtained from TEM analysis. The theoretical SAR as a function of particle size (Fig. 11(a)) and ESAR as a function of anisotropy energy (Fig. 11(b)) for polydispersions of Co0, Co1, and Co3 are represented as histograms. S_{avg} indicated using dashed lines in Fig. 11(a) and (b) is the average SAR and ESAR, in the respective plots computed using Eqs. (2) and (6). The theoretical results are proportionate to our experimental results. The histograms were fitted to suitable distributions and the average diameter for optimum SAR (D_{opt}) weighing polydispersions was computed. D_{opt} for Co0 is 13 nm, whereas, for Co1 and Co3, it is 12 nm. The narrow distribution in particle size and the lower K resulted in better heating efficiency for Co0 that falls under the LRT regime.

Although the average size of Co1 and Co3 matches with D_{opt}, the peak of Co3 in Fig. 11(a) seems to be much lower than Co1. This is in accordance with the theoretical simulation considering the particle size distribution and particles within the ambit of LRT. The decrease in SAR with magnetic anisotropy is once again demonstrated. In Fig. 11(b), the KV was deduced by substituting the K values estimated from ESR. Co0 and Co1, with the majority of MNPs in the low energy region, seem to exhibit better ESAR. Co3 presents a distribution of the significant number of MNPs in the high energy region, which accounts for the average ESAR closer to Co1. MNPs having lower anisotropy with an average particle diameter corresponding to the optimum size fall into the lower KV region and exhibit higher ESAR, whereas the high anisotropic particles present reduced ESAR.

Calculations of Carrey et al. [21] show that the maximum achievable SAR increases with a reduction in anisotropy for the nanoparticles of the same size since the volume is inversely proportional to anisotropy. However, this is applicable only to superparamagnetic nanoparticles that obey LRT. The T_B for Co-doped Fe_3O_4 with $x = 0.1$ reported by Mohapatra et al. [8] is 340 K, which means that the moments are entirely or partially blocked at room temperature. This sample is under the ferromagnetic regime and can only be explained by SWM rather than LRT. For the MNPs that obey SWM, the SAR increases with an increase in anisotropy, which was well observed by Fantechi et al. [7] and Mohapatra et al. [8]. The ESAR values estimated by us for the previously reported Co-doped Fe_3O_4 in the size range of 6–12 nm are between 0.05 and 1.53 nHm^2kg^{-1} [7,8,17,80–82]. These ESAR values are much smaller than 2.84–3.16 nHm^2kg^{-1} obtained in the present studies due to difference in the heating mechanism. The studies suggest a better heating rate with low K particles that are in the LRT regime or with reduced interparticle interaction.

4. Conclusions

Fe_3O_4 and Co-doped Fe_3O_4 nanoparticles with an average particle size of 10–12 nm show an enhancement in magnetic anisotropy constant from 16 to 31 kJm^{-3}, respectively. Infrared thermography has been used to probe the effective specific absorption rate (ESAR) of the nanoparticles. The specific absorption rates and magnetic properties reported in the literature were examined and reanalyzed comparing the ESAR. The Fe_3O_4 nanoparticles show an ESAR value of 3.16 nHm^2kg^{-1} that decreases up to 2.84 nHm^2kg^{-1} with Co-doping. The ESAR could be enhanced to 4.42 nHm^2kg^{-1} by reducing the interparticle interactions with dextran modification. The effect of ESAR on the particle size distribution has been estimated theoretically and compared with the experimental results. The decrease in heating for the Stoner-Wohlfarth particles with reducing size could be overcome by diminishing dipolar interaction strength. The results of this study propose surface-modified particles with low magnetic anisotropy that comply with linear response theory for better heating efficiency.

CRediT authorship contribution statement

J. Shebha Anandhi: Data curation, Formal analysis, Investigation, Resources, Software, Validation, Visualization, Writing - original draft, Writing - review & editing. **T. Arun:** Resources. **R. Justin Joseyphus:** Conceptualization, Methodology, Supervision, Writing - review & editing.

Declaration of competing interest

The authors declare that they have no known competing financial interests or personal relationships that could have appeared to influence the work reported in this paper.

Acknowledgments

The authors acknowledge the Department of Science and Technology (DST), Government of India for the experimental facilities, CRG project (CRG/2018/000939), Mr. G. Antilen Jacob, SAIF, IIT Bombay for ICP-AES, and SAIF, IIT Madras for ESR measurements.

References

[1] C.C. Berry, A.S.G. Curtis, Functionalisation of magnetic nanoparticles for applications in biomedicine, J. Phys. D Appl. Phys. 36 (2003) R198–R206, https://doi.org/10.1088/0022-3727/36/13/203.

[2] A.K. Gupta, M. Gupta, Synthesis and surface engineering of iron oxide nanoparticles for biomedical applications, Biomaterials 26 (2005) 3995–4021, https://doi.org/10.1016/j.biomaterials.2004.10.012.

[3] Q. Pankhurst, S. Jones, J. Dobson, Applications of magnetic nanoparticles in biomedicine: the story so far, J. Phys. D Appl. Phys. 49 (2016) 501002, https://doi.org/10.1088/0022-3727/49/50/501002.

[4] T. Hosono, H. Takahashi, A. Fujita, R.J. Joseyphus, K. Tohji, B. Jeyadevan, Synthesis of magnetite nanoparticles for AC magnetic heating, J. Magn. Magn Mater. 321 (2009) 3019–3023, https://doi.org/10.1016/j.jmmm.2009.04.061.

[5] R.E. Rosensweig, Heating magnetic fluid with alternating magnetic field, J. Magn. Magn Mater. 252 (2002) 370–374, https://doi.org/10.1016/s0304-8853(02)00706-0.

[6] P. Pradhan, J. Giri, G. Samanta, H.D. Sarma, K.P. Mishra, J. Bellare, R. Banerjee, D. Bahadur, Comparative evaluation of heating ability and biocompatibility of different ferrite-based magnetic fluids for hyperthermia application, J. Biomed. Mater. Res. B 81B (2007) 12–22, https://doi.org/10.1002/jbm.b.30630.

[7] E. Fantechi, C. Innocenti, M. Albino, E. Lottini, C. Sangregorio, Influence of cobalt doping on the hyperthermic efficiency of magnetite nanoparticles, J. Magn. Magn Mater. 380 (2015) 365–371, https://doi.org/10.1016/j.jmmm.2014.10.082.

[8] J. Mohapatra, M. Xing, J.P. Liu, Magnetic and hyperthermia properties of $Co_xFe_{3-x}O_4$ nanoparticles synthesized via cation exchange, AIP Adv. 8 (2018) 3–8, https://doi.org/10.1063/1.5006515.

[9] J.C. Slonczewski, Origin of magnetic anisotropy in cobalt-substituted magnetite, Phys. Rev. 110 (1958) 1341–1348, https://doi.org/10.1103/PhysRev.110.1341.

[10] B.D. Cullity, C.D. Graham (Eds.), Introduction to Magnetic Materials, second ed., John Wiley & Sons, Inc., New Jersey, 2009.

[11] H.S.C. O'Neill, A. Navrotsky, Simple spinels: crystallographic parameters, cation radii, lattice energies, and cation distribution, Am. Mineral. 68 (1983) 181–194.

[12] S. Bae, S.W. Lee, A. Hirukawa, Y. Takemura, Y.H. Jo, S.G. Lee, AC magnetic-field-induced heating and physical properties of ferrite nanoparticles for a hyperthermia agent in medicine, IEEE Trans. Nanotechnol. 8 (2009) 86–94, https://doi.org/10.1109/TNANO.2008.2007214.

[13] S. Dutz, R. Hergt, Magnetic particle hyperthermia - a promising tumour therapy? Nanotechnology 25 (2014) 452001, https://doi.org/10.1088/0957-4484/25/45/452001.

[14] V. Mameli, A. Musinu, A. Ardu, G. Ennas, D. Peddis, D. Niznansky, C. Sangregorio, C. Innocenti, N.T.K. Thanh, C. Cannas, Studying the effect of Zn-substitution on the magnetic and hyperthermic properties of cobalt ferrite nanoparticles, Nanoscale 8 (2016) 10124–10137, https://doi.org/10.1039/c6nr01303a.

[15] J.H. Lee, J.T. Jang, J.S. Choi, S.H. Moon, S.H. Noh, J.W. Kim, J.G. Kim, I.S. Kim, K. I. Park, J. Cheon, Exchange-coupled magnetic nanoparticles for efficient heat induction, Nat. Nanotechnol. 6 (2011) 418–422, https://doi.org/10.1038/nnano.2011.95.

[16] I. Andreu, E. Natividad, C. Ravagli, M. Castro, G. Baldi, Heating ability of cobalt ferrite nanoparticles showing dynamic and interaction effects, RSC Adv. 4 (2014) 28968–28977, https://doi.org/10.1039/c4ra02586e.

[17] J.P. Fortin, C. Wilhelm, J. Servais, C. Ménager, J.C. Bacri, F. Gazeau, Size-sorted anionic iron oxide nanomagnets as colloidal mediators for magnetic hyperthermia, J. Am. Chem. Soc. 129 (2007) 2628–2635, https://doi.org/10.1021/ja067457e.

[18] E. Kita, S. Hashimoto, T. Kayano, M. Minagawa, H. Yanagihara, M. Kishimoto, K. Yamada, T. Oda, N. Ohkohchi, T. Takagi, T. Kanamori, Y. Ikehata, I. Nagano, Heating characteristics of ferromagnetic iron oxide nanoparticles for magnetic hyperthermia, J. Appl. Phys. 107 (2010), 09B321, https://doi.org/10.1063/1.3355917.

[19] Q. Zhang, I. Castellanos-Rubio, R. Munshi, I. Orue, B. Pelaz, K.I. Gries, W.J. Parak, P. Del Pino, A. Pralle, Model driven optimization of magnetic anisotropy of exchange-coupled core-shell ferrite nanoparticles for maximal hysteretic loss, Chem. Mater. 27 (2015) 7380–7387, https://doi.org/10.1021/acs.chemmater.5b03261.

[20] E.L. Verde, G.T. Landi, J.A. Gomes, M.H. Sousa, A.F. Bakuzis, Magnetic hyperthermia investigation of cobalt ferrite nanoparticles: comparison between experiment, linear response theory, and dynamic hysteresis simulations, J. Appl. Phys. 111 (2012) 123902, https://doi.org/10.1063/1.4729271.

[21] J. Carrey, B. Mehdaoui, M. Respaud, Simple models for dynamic hysteresis loop calculations of magnetic single-domain nanoparticles: application to magnetic hyperthermia optimization, J. Appl. Phys. 109 (2011), 083921, https://doi.org/10.1063/1.3551582.

[22] J. Shebha Anandhi, G. Antilen Jacob, R. Justin Joseyphus, Factors affecting the heating efficiency of Mn-doped Fe_3O_4 nanoparticles, J. Magn. Magn Mater. 512 (2020) 166992, https://doi.org/10.1016/j.jmmm.2020.166992.

[23] J. Shebha Anandhi, G. Antilen Jacob, R. Justin Joseyphus, Heating characteristics of dextran modified magnetite nanoparticles by infrared thermography, Mater. Res. Express 6 (2019), 015045, https://doi.org/10.1088/2053-1591/aae87d.

[24] B.B. Lahiri, S. Ranoo, J. Philip, Magnetic hyperthermia study in water based magnetic fluids containing TMAOH coated Fe_3O_4 using infrared thermography, Infrared Phys. Technol. 80 (2017) 71–82, https://doi.org/10.1016/j.infrared.2016.11.015.

[25] H.F. Rodrigues, F.M. Mello, L.C. Branquinho, N. Zufelato, E.P. Silveira-Lacerda, A. F. Bakuzis, Real-time infrared thermography detection of magnetic nanoparticle hyperthermia in a murine model under a non-uniform field configuration, Int. J. Hyperther. 29 (2013) 752–767, https://doi.org/10.3109/02656736.2013.839056.

[26] S.S. Pati, S. Gopinath, G. Panneerselvam, M.P. Antony, J. Philip, High temperature phase transformation studies in magnetite nanoparticles doped with Co^{2+} ion, J. Appl. Phys. 112 (2012), 054320, https://doi.org/10.1063/1.4748318.

[27] J.M. Byrne, V.S. Coker, S. Moise, P.L. Wincott, D.J. Vaughan, F. Tuna, E. Arenholz, G. van der Laan, R.A.D. Pattrick, J.R. Lloyd, N.D. Telling, Controlled cobalt doping in biogenic magnetite nanoparticles, J. R. Soc. Interface 10 (2013) 20130134, https://doi.org/10.1098/rsif.2013.0134.

[28] J.B. Yang, X.D. Zhou, W.B. Yelon, W.J. James, Q. Cai, K.V. Gopalakrishnan, S. K. Malik, X.C. Sun, D.E. Nikles, Magnetic and structural studies of the Verwey transition in $Fe_{3-\delta}O_4$ nanoparticles, J. Appl. Phys. 95 (2004) 7540–7542, https://doi.org/10.1063/1.1669344.

[29] A. Demortière, P. Panissod, B.P. Pichon, G. Pourroy, D. Guillon, B. Donnio, S. Bégin-Colin, Size-dependent properties of magnetic iron oxide nanocrystals, Nanoscale 3 (2011) 225–232, https://doi.org/10.1039/c0nr00521e.

[30] A. Hartridge, A.K. Bhattacharya, M. Sengupta, C.K. Majumdar, D. Das, S. N. Chintalapudi, Crystallite size dependence on the magnetic properties of nanocrystalline magnetite powders, J. Magn. Magn Mater. 176 (1997) 6–9, https://doi.org/10.1016/S0304-8853(97)01004-4.

[31] J.M. Shaw, H.T. Nembach, T.J. Silva, C.T. Boone, Precise determination of the spectroscopic g-factor by use of broadband ferromagnetic resonance spectroscopy, J. Appl. Phys. 114 (2013) 243906, https://doi.org/10.1063/1.4852415.

[32] P.C. Fannin, I. Malaescu, C.N. Marin, The effective anisotropy constant of particles within magnetic fluids as measured by magnetic resonance, J. Magn. Magn Mater. 289 (2005) 162–164, https://doi.org/10.1016/j.jmmm.2004.11.047.

[33] E. De Biasi, E. Lima, C.A. Ramos, A. Butera, R.D. Zysler, Effect of thermal fluctuations in FMR experiments in uniaxial magnetic nanoparticles: blocked vs. superparamagnetic regimes, J. Magn. Magn Mater. 326 (2013) 138–146, https://doi.org/10.1016/j.jmmm.2012.08.046.

[34] H. Li, M.T. Klem, K.B. Sebby, D.J. Singel, M. Young, T. Douglas, Y.U. Idzerda, Determination of anisotropy constants of protein encapsulated iron oxide nanoparticles by electron magnetic resonance, J. Magn. Magn Mater. 321 (2009) 175–180, https://doi.org/10.1016/j.jmmm.2008.08.082.

[35] Y. Köseoğlu, Effect of surfactant coating on magnetic properties of Fe_3O_4 nanoparticles: ESR study, J. Magn. Magn Mater. 300 (2006) 327–330, https://doi.org/10.1016/j.jmmm.2005.10.112.

[36] O. Ayala-Valenzuela, P.C. Fannin, R. Betancourt-Galindo, O. Rodríguez-Fernández, J. Matutes-Aquino, Characterization of different magnetite-cobalt nanoparticles in hydrocarbon-based magnetic fluids by means of static and dynamic magnetization measurements, J. Magn. Magn Mater. 311 (2007) 111–113, https://doi.org/10.1016/j.jmmm.2006.10.1198.

[37] R.S. Van Dyck, P.B. Schwinberg, H.G. Dehmelt, New high-precision comparison of electron and positron g factors, Phys. Rev. Lett. 59 (1987) 26–29, https://doi.org/10.1103/physrevlett.59.26.

[38] J.S. Miller, M. Drillon (Eds.), Magnetism: Molecules to Materials IV, Wiley-VCH, Weinheim, 2002, https://doi.org/10.1002/9783527620548.

[39] R.H. Kodama, A.E. Berkowitz, E.J. McNiff Jr., S. Foner, Surface spin disorder in $NiFe_2O_4$ nanoparticles, Phys. Rev. Lett. 77 (1996) 394–397, https://doi.org/10.1103/physrevlett.77.394.

[40] C.N. Chinnasamy, B. Jeyadevan, K. Shinoda, K. Tohji, D.J. Djayaprawira, M. Takahashi, R. Justin Joseyphus, A. Narayanasamy, Unusually high coercivity and critical single-domain size of nearly monodispersed CoFe2O4 nanoparticles, Appl. Phys. Lett. 83 (2003) 2862–2864, https://doi.org/10.1063/1.1616655.

[41] I.C. Nlebedim, J.E. Snyder, A.J. Moses, D.C. Jiles, Anisotropy and magnetostriction in non-stoichiometric cobalt ferrite, IEEE Trans. Magn. 48 (2012) 3084–3087, https://doi.org/10.1109/TMAG.2012.2200884.

[42] S. Yoon, Temperature dependence of magnetic anisotropy constant in cobalt ferrite nanoparticles, J. Magn. Magn Mater. 324 (2012) 2620–2624, https://doi.org/10.1016/j.jmmm.2012.03.019.

[43] T. Arun, K. Prakash, R. Kuppusamy, R.J. Joseyphus, Magnetic properties of prussian blue modified Fe_3O_4 nanocubes, J. Phys. Chem. Solid. 74 (2013) 1761–1768, https://doi.org/10.1016/j.jpcs.2013.07.005.

[44] G.A. Jacob, S. Sellaiyan, A. Uedono, R.J. Joseyphus, Magnetic properties of metastable bcc phase in $Fe_{64}Ni_{36}$ alloy synthesized through polyol process, Appl. Phys. A 126 (2020) 1–7, https://doi.org/10.1007/s00339-020-3292-3.

[45] E. De Grave, R.M. Persoons, R.E. Vandenberghe, P.M.A. de Bakker, Mössbauer study of the high-temperature phase of Co-substituted magnetites, $Co_xFe_{3-x}O_4$. I. $x \leq 0.04$, Phys. Rev. B 47 (1993) 5881–5893, https://doi.org/10.1103/physrevb.47.5881.

[46] R. Kodama, Magnetic nanoparticles, J. Magn. Magn Mater. 200 (1999) 359–372, https://doi.org/10.1016/s0304-8853(99)00347-9.

[47] D. Durneata, R. Hempelmann, O. Caltun, I. Dumitru, High-frequency specific absorption rate of $Co_xFe_{1-x}Fe_2O_4$ Ferrite nanoparticles for hypertermia applications, IEEE Trans. Magn. 50 (2014) 4–7, https://doi.org/10.1109/TMAG.2014.2324011.

[48] S.A. Majetich, M. Sachan, Magnetostatic interactions in magnetic nanoparticle assemblies: energy, time and length scales, J. Phys. D Appl. Phys. 39 (2006) R407–R422, https://doi.org/10.1088/0022-3727/39/21/R02.

[49] D. Peddis, F. Orrù, A. Ardu, C. Cannas, A. Musinu, G. Piccaluga, Interparticle interactions and magnetic anisotropy in cobalt ferrite nanoparticles: influence of molecular coating, Chem. Mater. 24 (2012) 1062–1071, https://doi.org/10.1021/cm203280y.

[50] S.L. Saville, B. Qi, J. Baker, R. Stone, R.E. Camley, K.L. Livesey, L. Ye, T. M. Crawford, O. Thompson Mefford, The formation of linear aggregates in magnetic hyperthermia: implications on specific absorption rate and magnetic anisotropy, J. Colloid Interface Sci. 424 (2014) 141–151, https://doi.org/10.1016/j.jcis.2014.03.007.

[51] D. Kechrakos, K. Trohidou, Magnetic properties of dipolar interacting single-domain particles, Phys. Rev. B Condens. Matter 58 (1998) 12169–12177, https://doi.org/10.1103/PhysRevB.58.12169.
[52] D.C. Lee, F.V. Mikulec, J.M. Pelaez, B. Koo, B.A. Korgel, Synthesis and magnetic properties of silica-coated FePt nanocrystals, J. Phys. Chem. B 110 (2006) 11160–11166, https://doi.org/10.1021/jp060974z.
[53] D. Niculaes, A. Lak, G.C. Anyfantis, S. Marras, O. Laslett, S.K. Avugadda, M. Cassani, D. Serantes, O. Hovorka, R. Chantrell, T. Pellegrino, Asymmetric assembling of iron oxide nanocubes for improving magnetic hyperthermia performance, ACS Nano 11 (2017) 12121–12133, https://doi.org/10.1021/acsnano.7b05182.
[54] M. Palihawadana-Arachchige, H. Nemala, V.M. Naik, R. Naik, Effect of magnetic dipolar interactions on temperature dependent magnetic hyperthermia in ferrofluids, J. Appl. Phys. 121 (2017), 023901, https://doi.org/10.1063/1.4973879.
[55] C. Blanco-Andujar, A. Walter, G. Cotin, C. Bordeianu, D. Mertz, D. Felder-Flesch, S. Begin-Colin, Design of iron oxide-based nanoparticles for MRI and magnetic hyperthermia, Nanomedicine 11 (2016) 1889–1910, https://doi.org/10.2217/nnm-2016-5001.
[56] C. Martinez-Boubeta, K. Simeonidis, A. Makridis, M. Angelakeris, O. Iglesias, P. Guardia, A. Cabot, L. Yedra, S. Estradé, F. Peiró, Z. Saghi, P.A. Midgley, I. Conde-Leborán, D. Serantes, D. Baldomir, Learning from nature to improve the heat generation of iron-oxide nanoparticles for magnetic hyperthermia applications, Sci. Rep. 3 (2013) 1–8, https://doi.org/10.1038/srep01652.
[57] D.E. Bordelon, C. Cornejo, C. Grttner, F. Westphal, T.L. Deweese, R. Ivkov, Magnetic nanoparticle heating efficiency reveals magneto-structural differences when characterized with wide ranging and high amplitude alternating magnetic fields, J. Appl. Phys. 109 (2011) 124904, https://doi.org/10.1063/1.3597820.
[58] R. Hergt, W. Andra, C.G. d'Ambly, I. Hilger, W.A. Kaiser, U. Richter, H.-G. Schmidt, Physical limits of hyperthermia using magnetite fine particles, IEEE Trans. Magn. 34 (1998) 3745–3754, https://doi.org/10.1109/20.718537.
[59] R. Hergt, S. Dutz, M. Röder, Effects of size distribution on hysteresis losses of magnetic nanoparticles for hyperthermia, J. Phys. Condens. Matter 20 (2008) 385214, https://doi.org/10.1088/0953-8984/20/38/385214.
[60] S. Laurent, S. Dutz, U.O. Häfeli, M. Mahmoudi, Magnetic fluid hyperthermia: focus on superparamagnetic iron oxide nanoparticles, Adv. Colloid Interface Sci. 166 (2011) 8–23, https://doi.org/10.1016/j.cis.2011.04.003.
[61] X.L. Liu, H.M. Fan, J.B. Yi, Y. Yang, E.S.G. Choo, J.M. Xue, D. Di Fan, J. Ding, Optimization of surface coating on Fe_3O_4 nanoparticles for high performance magnetic hyperthermia agents, J. Mater. Chem. 22 (2012) 8235–8244, https://doi.org/10.1039/c2jm30472d.
[62] A. Jordan, R. Scholz, P. Wust, H. Schirra, Thomas Schiestel, H. Schmidt, R. Felix, Endocytosis of dextran and silan-coated magnetite nanoparticles and the effect of intracellular hyperthermia on human mammary carcinoma cells in vitro, J. Magn. Magn Mater. 194 (1999) 185–196, https://doi.org/10.1016/s0304-8853(98)00558-7.
[63] S. Dutz, R. Hergt, Magnetic nanoparticle heating and heat transfer on a microscale: basic principles, realities and physical limitations of hyperthermia for tumour therapy, Int. J. Hyperther. 29 (2013) 790–800, https://doi.org/10.3109/02656736.2013.822993.
[64] R. Ramprasad, P. Zurcher, M. Petras, M. Miller, P. Renaud, Magnetic properties of metallic ferromagnetic nanoparticle composites, J. Appl. Phys. 96 (2004) 519–529, https://doi.org/10.1063/1.1759073.
[65] P. De La Presa, Y. Luengo, M. Multigner, R. Costo, M.P. Morales, G. Rivero, A. Hernando, Study of heating efficiency as a function of concentration, size, and applied field in γ-Fe_2O_3 nanoparticles, J. Phys. Chem. C 116 (2012) 25602–25610, https://doi.org/10.1021/jp310771p.
[66] B. Jeyadevan, Present status and prospects of magnetite nanoparticles-based hyperthermia, J. Ceram. Soc. Japan. 118 (2010) 391–401, https://doi.org/10.2109/jcersj2.118.391.
[67] A. Józefczak, B. Leszczyński, A. Skumiel, T. Hornowski, A comparison between acoustic properties and heat effects in biogenic (magnetosomes) and abiotic magnetite nanoparticle suspensions, J. Magn. Magn Mater. 407 (2016) 92–100, https://doi.org/10.1016/j.jmmm.2016.01.054.
[68] M. Kallumadil, M. Tada, T. Nakagawa, M. Abe, P. Southern, Q.A. Pankhurst, Suitability of commercial colloids for magnetic hyperthermia, J. Magn. Magn Mater. 321 (2009) 1509–1513, https://doi.org/10.1016/j.jmmm.2009.02.075.
[69] M.A. Gonzalez-Fernandez, T.E. Torres, M. Andrés-Vergés, R. Costo, P. de la Presa, C.J. Serna, M.P. Morales, C. Marquina, M.R. Ibarra, G.F. Goya, Magnetic nanoparticles for power absorption: optimizing size, shape and magnetic properties, J. Solid State Chem. 182 (2009) 2779–2784, https://doi.org/10.1016/j.jssc.2009.07.047.
[70] B.B. Lahiri, S. Ranoo, J. Philip, Infrared thermography based magnetic hyperthermia study in Fe_3O_4 based magnetic fluids, Infrared Phys. Technol. 78 (2016) 173–184, https://doi.org/10.1016/j.infrared.2016.08.002.
[71] B.B. Lahiri, S. Ranoo, J. Philip, Uncertainties in the estimation of specific absorption rate during radiofrequency alternating magnetic field induced non-adiabatic heating of ferrofluids, J. Phys. D Appl. Phys. 50 (2017) 455005, https://doi.org/10.1088/1361-6463/aa89de.
[72] M. Suto, H. Kosukegawa, K. Maruta, M. Ohta, K. Tohji, B. Jeyadevan, Heat diffusion characteristics of magnetite nanoparticles dispersed hydro-gel in alternating magnetic field, J. Magn. Magn Mater. 321 (2009) 3483–3487, https://doi.org/10.1016/j.jmmm.2009.06.067.
[73] L.C. Branquinho, M.S. Carrião, A.S. Costa, N. Zufelato, M.H. Sousa, R. Miotto, R. Ivkov, A.F. Bakuzis, Effect of magnetic dipolar interactions on nanoparticle heating efficiency: implications for cancer hyperthermia, Sci. Rep. 3 (2013) 20–22, https://doi.org/10.1038/srep02887.
[74] R.D. Raland, J.P. Borah, Efficacy of heat generation in CTAB coated Mn doped $ZnFe_2O_4$ nanoparticles for magnetic hyperthermia, J. Phys. D Appl. Phys. 50 (2017), 035001, https://doi.org/10.1088/1361-6463/aa4e9a.
[75] G. Salas, J. Camarero, D. Cabrera, H. Takacs, M. Varela, R. Ludwig, H. Dähring, I. Hilger, R. Miranda, M.D.P. Morales, F.J. Teran, Modulation of magnetic heating via dipolar magnetic interactions in monodisperse and crystalline iron oxide nanoparticles, J. Phys. Chem. C 118 (2014) 19985–19994, https://doi.org/10.1021/jp5041234.
[76] K. Wu, J.P. Wang, Magnetic hyperthermia performance of magnetite nanoparticle assemblies under different driving fields, AIP Adv. 7 (2017), 056327, https://doi.org/10.1063/1.4978458.
[77] J. Zhang, C. Boyd, W. Luo, Two mechanisms and a scaling relation for dynamics in ferrofluids, Phys. Rev. Lett. 77 (1996) 390–393, https://doi.org/10.1103/physrevlett.77.390.
[78] M.C. Franchini, G. Baldi, D. Bonacchi, D. Gentili, G. Giudetti, A. Lascialfari, M. Corti, P. Marmorato, J. Ponti, E. Micotti, U. Guerrini, L. Sironi, P. Gelosa, C. Ravagli, A. Ricci, Bovine serum albumin-based magnetic nanocarrier for MRI diagnosis and hyperthermic therapy: a potential theranostic approach against cancer, Small 6 (2010) 366–370, https://doi.org/10.1002/smll.200901689.
[79] G.T. Landi, Role of dipolar interaction in magnetic hyperthermia, Phys. Rev. B 89 (2014) 1–6, https://doi.org/10.1103/PhysRevB.89.014403.
[80] E. Fantechi, C. Innocenti, M. Zanardelli, M. Fittipaldi, E. Falvo, M. Carbo, V. Shullani, L. Di Cesare Mannelli, C. Ghelardini, A.M. Ferretti, A. Ponti, C. Sangregorio, P. Ceci, A smart platform for hyperthermia application in cancer treatment: cobalt-doped ferrite nanoparticles mineralized in human ferritin cages, ACS Nano 8 (2014) 4705–4719, https://doi.org/10.1021/nn500454n.
[81] M. Gonzales-Weimuller, M. Zeisberger, K.M. Krishnan, Size-dependant heating rates of iron oxide nanoparticles for magnetic fluid hyperthermia, J. Magn. Magn Mater. 321 (2009) 1947–1950, https://doi.org/10.1016/j.jmmm.2008.12.017.
[82] P.H. Linh, N.T.N. Anh, P.H. Nam, T.N. Bach, V.D. Lam, D.H. Manh, A facile ultrasound assisted synthesis of dextran-stabilized $Co_{0.2}Fe_{0.8}Fe_2O_4$ nanoparticles for hyperthermia application, IEEE Trans. Magn. 54 (2018) 1–4, https://doi.org/10.1109/tmag.2018.2815080.